CO oxidation and COPrOx over preformed Au nanoparticles supported over nanoshaped CeO$_2$

Lluís Soler[1], Albert Casanovas[1], Aitor Urrich[1], Inmaculada Angurell[2] and Jordi Llorca[1,*]

[1]Institute of Energy Technologies and Centre for Research in Nanoengineering, Universitat Politècnica de Catalunya, Diagonal 647, ed. ETSEIB, 08028 Barcelona, Spain.

[2]Department of Inorganic Chemistry, Universitat de Barcelona, Martí i Franquès 1, 08028 Barcelona, Spain.

[*]Corresponding author:

Prof. Jordi Llorca
Institut de Tècniques Energètiques,
Universitat Politècnica de Catalunya
Av. Diagonal 647, Ed. ETSEIB
08028 Barcelona, Spain
Tel.: (+34) 93 401 17 08
e-mail: jordi.llorca@upc.edu

Abstract

Au/CeO$_2$ (0.25% wt. Au) catalysts were prepared by anchoring preformed Au nanoparticles over ceria polycrystals, cubes and rods and tested in the oxidation of CO and COPrOx. The use of preformed Au nanoparticles assured a constant Au particle size (ca. 5 nm by HRTEM) for all samples, which allowed to a precise assessment of the effect of the morphology of nanoshaped ceria on catalytic activity. The catalytic performance of the Au/CeO$_2$-rods was much better than that of the Au/CeO$_2$-polycrystals and Au/CeO$_2$-cubes both in the oxidation of CO and COPrOx reactions. The Au/CeO$_2$-rods exhibited the highest amount of oxidized Au and Ce(III) species by XPS, whereas in the Au/CeO$_2$-cubes gold was totally metallic and the amount of Ce(III) was minimum. An intermediate situation was encountered in the Au/CeO$_2$-polycrystals. Considering the differences in the oxidation states of Au and Ce and the fact that all samples were prepared with preformed metallic Au nanoparticles of the same size, the results indicate that the intrinsic nature of the different ceria surfaces exerts a prominent role in the gold-ceria interaction and in the electron density transfer from Au to Ce, which in turn has a strong effect on catalytic activity. Gold nanoparticles strongly interact with CeO$_2$-{110} surfaces with respect to CeO$_2$-{111} and CeO$_2$-{100}, even when Au nanoparticles are prepared separately and simply deposited by impregnation.

Keywords

1. Introduction

The oxidation of carbon monoxide (CO) and, in particular, its preferential oxidation in the presence of large quantities of hydrogen (H_2) represents a very important aspect of fuel cell technology and the development of processes devoted to obtain CO-free hydrogen streams is a critical issue and an essential requirement for feeding proton exchange membrane fuel cells (PEMFC) [1]. Carbon monoxide preferential oxidation (COPrOx) is particularly appealing when applied to low-scale or portable reformer-PEMFC systems due to its fairly simple implementation, low operation costs and minimal loss of hydrogen [2–4]. In the COPrOx, two oxidation reactions compete for the oxygen consumption and, as a consequence, COPrOx catalysts have to exhibit high CO oxidation activity, while H_2 oxidation has to be maintained low in order to avoid fuel losses, at temperatures ranging from 80 to 200°C. A profuse number of studies on the design of suitable catalysts for the competitive oxidation of CO in the presence of H_2 have been published. Among them, supported Au catalysts exhibit exceptionally high CO oxidation activity in the low-temperature range when gold is dispersed as particles with diameters smaller than 5 nm [5–11].

Ceria is a key component for many oxidation catalysts and its catalytic activity shows a strong dependence on morphology [12,13]. The shape-dependent activity of ceria has been recognized not only in the catalytic oxidation of CO [14–21], but also on NO reduction [22], water-gas shift reaction [23–25], reforming reactions [26–29] and soot combustion [30]. Polycrystalline ceria nanoparticles usually consist of octahedra or truncated octahedron shapes, which mainly expose the most stable {111} facets in order to minimize surface energy, whereas nanorods are terminated by {110} and {100} planes and nanocubes expose {100} surfaces. The energy required to form oxygen vacancies on the {111} surface of CeO_2 is higher than those on {110} and {100} surfaces, so there are more oxygen vacancies on {110} and {100} planes [31]. As the number of vacancies increases, the movement of oxygen atoms in the lattice becomes

easier, and the increased diffusion rate of oxygen in the lattice results in increased catalytic activity [32]. Accordingly, the reactivity of nanoshaped ceria rods and cubes for the oxidation of CO is higher than that of the ceria polycrystals [33–35].

When considering Au/CeO_2 catalysts, the emergence of various ceria nanoshapes should enable the study of the CeO_2 morphology on the metal-oxide interaction and catalytic activity, but in spite of numerous studies in this field [36–38], the nature of the Au-oxide interface remains a controversial issue. The main problem is the formation of different Au ensembles and structures over the different ceria nanoshapes arising from the preparation methods and/or pretreatments, which exhibit different intrinsic reactivity per se. Data clearly show that the morphology of ceria strongly affects the structure of gold nanoparticles prepared from Au salts [39]. Very often, CeO_2 rods stabilize Au atoms and clusters whereas Au nanoparticles are found in Au/CeO_2 cubes [40,41]. In this way, the discussion about the influence of ceria nanoshapes on catalytic activity is masked by different gold particle sizes and structures, which are critical factors for catalytic activity. To overcome this difficulty, in this work we study the CO oxidation and COPrOx reaction over preformed Au metal nanoparticles supported on ceria nanocubes, nanorods and nanopolyhedra in an effort to elucidate the precise role of the nanoshape of the ceria support. The use of preformed Au nanoparticles guarantees the same Au particle size and a similar architecture of the Au-support interaction for all the samples tested, so the effects of the ceria nanoshape on catalytic performance can be properly investigated [42,43].

2. Experimental

2.1 Catalyst preparation

Conventional CeO_2 polycrystals (CeO_2-p) were prepared by precipitation adding 35 ml of an aqueous solution of 0.4 M $Ce(NO_3)_3 \cdot 6H_2O$ using an electrospray (Digital

Ultrasonic Atomizer, Sonaer Inc.) to create a fine aerosol of liquid droplets into 245 ml of a 0.2 M NaOH solution under vigorous stirring. The resultant suspension was kept under agitation for 30 minutes. Then, the suspension was transferred into a PTFE-lined cylinder and sealed in a stainless steel autoclave and heated at 423 K for 24 h. After cooling, the resulting mixture was centrifuged and washed three times with deionized water and three times with ethanol for separation and purification of the powder, which was dried at 333 K overnight. Ceria nanocubes (CeO_2-c), and nanorods (CeO_2-r) were prepared as reported elsewhere in detail [44]. Briefly, they were synthesized adding 35 ml of an aqueous solution of 0.4 M $Ce(NO_3)_3 \cdot 6H_2O$ by means of an electrospray into 245 ml of a 6.9 M NaOH solution for CeO_2-c and 9.0 M NaOH solution for CeO_2-r, under vigorous stirring for 30 minutes. The suspension of CeO_2-c was heated at 453 K for 24 h, and the suspension of CeO_2-r was heated at 373 K for 24 h. After cooling, the resulting mixtures were processed as described above for CeO_2-p.

The preparation of the model Au nanoparticles was reported in detail in [45]. They were synthesized following the two-phase method described for the synthesis of dodecanethiol-capped monometallic Au nanoparticles [46], which involved the transfer of $AuCl_4^-$ to a toluene solution using tetraoctylammonium bromide followed by a single reduction step with $NaBH_4$ in the presence of dodecanethiol. The Au/CeO_2 catalysts (0.25% wt. Au) were prepared by incipient wetness impregnation from a toluene solution (the solution was homogenized and divided in three parts) containing the model Au nanoparticles (40 mM) over CeO_2 polycrystals, nanocubes and nanorods (Au/CeO_2-p, Au/CeO_2-c and Au/CeO_2-r, respectively). Samples were calcined at 673 K for 4 h to remove the protecting shell.

2.2 Catalyst characterization

Scanning electron microscopy (SEM) images were recorded at 5 kV using a Zeiss Neon40 Crossbeam Station instrument equipped with a field emission source. The free software Fiji was used to measure the particle size of the samples. About two hundred particles were considered for particle size distribution estimation. High resolution transmission electron microscopy (HRTEM) was carried out using a JEOL 2010F electron microscope equipped with a field emission source at an accelerating voltage of 200 kV. Samples were deposited on holey carbon-coated grids. The point-to-point resolution achieved was 0.19 nm and the resolution between lines was 0.14 nm. The average particle diameter was calculated from the mean diameter frequency distribution with the formula: $d = \Sigma n_i d_i / \Sigma n_i$, where n_i is the number of particles with particle diameter d_i in a certain range.

Nitrogen adsorption isotherms were performed at 77 K using a Micromeritics ASAP2020 gas adsorption instrument. The materials were degassed at 473 K for 10 h prior to the adsorption experiments. The specific surface areas were calculated using the Brunauer-Emmett-Teller (BET) method. The Au content of the samples was determined by an inductively coupled plasma-optical emission spectrometry (ICP-OES) using a Perkin Elmer Optima 3200RL.

X-ray photoelectron spectroscopy (XPS) was performed on a SPECS system equipped with an Al anode XR50 source operating at 150 mW and a Phoibos MCD-9 detector. The pass energy of the hemispherical analyzer was set at 25 eV and the energy step was set at 0.1 eV. The pressure in the analysis chamber was kept below 10^{-7} Pa. The area analyzed was about 2 mm x 2 mm. Data processing was performed with the CasaXPS program (Casa Software Ltd., UK). Atomic fractions were calculated using peak areas normalized on the basis of acquisition parameters after background subtraction, experimental sensitivity factors and transmission factors provided by the manufacturer. Cerium 3d spectra were deconvoluted using six peaks for Ce^{4+} (V, V'', V''', U, U'' and U'''), corresponding to three pairs of spin-orbit doublets and four peaks

for Ce^{3+} (V_0, V', U_0 and U'), which correspond to two doublets, based on the peak positions reported by Mullins et al. [47], where U and V refer to the $3d_{3/2}$ and $3d_{5/2}$ spin-orbit components, respectively.

2.3 Catalytic tests

The oxidation of CO and COPrOx reactions were performed at 296-453 K and atmospheric pressure in a lab-scale set up. All the samples were tested following the same procedure, consisting in a first CO oxidation cycle, starting from room temperature (296-298 K) and increasing the reactor temperature in steps of 20 K until steady state was reached and up to a temperature of 453 K. Then, the reactor was cooled down overnight to room temperature and a second COPrOx reaction cycle was performed, following the same temperature profile of the first test. A total flow of 100 ml·min^{-1} of two different gaseous mixtures (CO:O_2:N_2=1:1:48 molar for CO oxidation or CO:O_2:N_2:H_2=1:1:23:25 molar for COPrOx experiments) was used to evaluate the performance of all the CeO_2 supports and the Au/CeO_2 catalysts. A tubular reactor was loaded with a mixture of 0.1g of powdered sample intimately mixed with granulated cordierite to achieve a total volume of ca. 2.6 cm^3, which led to a GHSV of 2300 h^{-1}. The gaseous effluent stream was quantitatively evaluated in terms of volumetric total flowrate (bubble soap meter) and composition. A gas chromatograph (Micro GC Agilent 3000A) equipped with MS 5A, Plot U and Stabilwax capillary columns and TCD detectors was used to measure on-line gas concentrations every 5 min. The products of the reaction were CO_2 and H_2O (no CH_4 was detected), and the remaining CO, O_2 and H_2 reactants were also measured. Outlet molar flowrates of the non-condensable components (H_2, CO_2, CO and O_2) were determined from the measured composition by GC and the total volumetric flowrate of the gaseous outlet stream, whereas outlet flowrate of H_2O was evaluated by closing element balances. The CO conversion (χ_{CO}) was calculated using the equation (1), where n_{COin} is the inlet molar flowrate of CO,

n_{COout} is the outer molar flowrate of CO that has not been reacted and n_{CO2out} is the outlet molar flowrate of the produced CO_2 during the experiment:

$$\chi_{CO}(\%) = \frac{n_{COin} - n_{COout}}{n_{COin}} \cdot 100 = \frac{n_{CO_2out}}{n_{COin}} \cdot 100 \tag{1}$$

The CO oxidation rate (in $mol \cdot h^{-1} \cdot m^{-2}$) of the different nanoshaped ceria supports was calculated normalizing the n_{CO2out} (in $mol \cdot h^{-1}$) by its corresponding BET surface area. Finally, the CO selectivity in COPrOx experiments was calculated using equation (2), where n_{H2in} is the inlet molar flowrate of H_2 and n_{H2out} is the outer molar flowrate of H_2 that has not been reacted:

$$S_{CO}(\%) = \frac{n_{COin} - n_{COout}}{(n_{COin} - n_{COout}) + (n_{H_2in} - n_{H_2out})} \cdot 100 \tag{2}$$

3. Results and discussion

3.1 Microstructural characterization

The morphology of the different ceria nanoshapes was studied by SEM whereas their structure and that of Au/CeO_2 counterparts were analyzed by HRTEM. Figure 1 illustrates representative SEM images of the ceria supports. Ceria nanocubes, CeO_2-c, (Figure 1A) ranged from about 15 to 30 nm in size and exhibited sharp edges in accordance to their cubic morphology. Occasionally, larger nanocubes up to 120 nm were also observed. The BET surface area measured for the CeO_2-c sample was 33 $m^2 \cdot g^{-1}$. Figure 1B corresponds to ceria polycrystals, CeO_2-p, which measured about 5-15 nm and were round-shaped. Accordingly, the BET surface area of the CeO_2-p sample was higher, 60 $m^2 \cdot g^{-1}$. Figure 1C shows the ceria nanorods, CeO_2-r, which were 10-15 nm in diameter and roughly 0.2-0.5 μm in length. The BET surface area measured for the CeO_2-r sample was 70 $m^2 \cdot g^{-1}$. Further SEM observations of the

samples after impregnation with the preformed Au nanoparticles and calcination did not show significant differences concerning the ceria support morphologies.

The same batches of ceria nanoshaped samples as prepared were studied in detail by HRTEM as well as after deposition of Au preformed nanoparticles (Figure 2). Figure 2A corresponds to the CeO_2-p sample. The sample was constituted by ceria nanoparticles perfectly crystalline exhibiting well-defined lattice fringes. The Fourier Transform (FT) image contains rings due to the numerous ceria crystallites present in the HRTEM image with multiple orientations. They are located at 3.1, 2.7, 1.9 and 1.6 Å, which match perfectly the (111), (200), (220) and (311) crystallographic planes of the fcc CeO_2 structure. The ceria crystallites exhibited various facets, but {111} terminations were dominant. Figure 2B shows a representative image of the Au/CeO_2-p sample along with an enlargement and a FT image of the area enclosed within the white square. A detailed lattice fringe analysis reveals the presence of an Au nanoparticle exhibiting a lattice spacing at 2.0 Å, which is ascribed to the (200) crystallographic planes of metallic Au. The Au nanoparticle is fixed over a ceria crystallite showing lattice fringes at 3.1 Å, which correspond to the (111) crystallographic planes of CeO_2. The spots at 2.3 Å in the FT image correspond to (111) crystallographic planes of metallic Au. Gold nanoparticles were round-shaped and their particle size was very homogeneous in the range 4.5-5.5 nm. Figure 2C corresponds to the CeO_2-c sample. As expected from SEM, the HRTEM image shows perfectly cubic ceria particles with {100} facets and lattice fringes at 2.7 Å corresponding to the (200) crystallographic planes of fcc CeO_2. The FT pattern in the inset shows the characteristic cubic pattern of cubic ceria oriented along the [100] crystallographic direction. As expected, there was no structural change after Au deposition (Figure 2D), and the morphology of the ceria nanocubes was preserved after the impregnation and calcination steps during the preparation of the catalyst. Again, the Au nanoparticles were round-shaped, well dispersed over the ceria support, and measured 4.5-5.5 nm in diameter. Figure 2E

corresponds to the CeO$_2$-r sample. The sample was constituted by well-defined ceria nanorods exhibiting mostly {110} facets. The deposition of Au preformed nanoparticles over the ceria nanorods resulted in a catalyst with the same nanorod morphology decorated with individual Au nanoparticles measuring 4.5-5.5 nm in diameter. The inset in Figure 2F shows a representative Au nanoparticle in the Au/CeO$_2$-r sample, which exhibits lattice fringes at 2.3 and 2.0 Å, which are ascribed to the (111) and (200) crystallographic planes of metallic Au, respectively. The Au loading contents over nanoshaped ceria samples were determined to be 0.25±0.02. Additionally, further HRTEM observations of used Au/CeO$_2$ samples after the second COPrOx reaction cycle (296-453 K) indicated that there were no changes in the nanoshapes and crystallographic planes of the ceria supports, and Au nanoparticles kept the same average size of 4.5-5.5 nm after the reaction. Au displacement from the ceria supports or Au sintering phenomena were also not observed (Fig. S1, Supplementary content).

Therefore, the use of preformed Au nanoparticles allowed us to prepare Au/CeO$_2$ catalysts with different ceria morphologies but with exactly the same Au particle size. Then, we have a set of catalysts that differ in the ceria facets exposed but contain a similar number of Au-ceria contact points. Consequently, we can attempt to provide an accurate analysis of the effect of the ceria nanoshape on the catalytic performance of Au/CeO$_2$ catalysts without introducing other structural effects due to the Au nanoparticles themselves, or to a different Au-ceria architecture.

3.2 CO oxidation and COPrOx

Concerning CO oxidation, the experimental data of conversion of CO for the different Au/CeO$_2$ nanoshapes are plotted in Figure 3A, based on equal sample weight and Au content in the reactor. It should be recalled that a direct comparison is possible since the use of preformed Au nanoparticles allows for preparing samples with exactly the

same number of Au-ceria contact points, independently of the ceria surface area. The obtained results clearly indicate that the oxidation of CO over preformed Au nanoparticles supported on nanoshaped ceria follows the order of Au/CeO_2-r > Au/CeO_2-p > Au/CeO_2-c. For instance, the temperature for half-conversion (T_{50}) of CO is 361 K for Au/CeO_2-r, 405 K for Au/CeO_2-p and 427 K for Au/CeO_2-c. Since the content and size of the Au nanoparticles is exactly the same for each sample, the exhibited behavior of nanoshaped Au/CeO_2 samples implies that the morphology of the support plays a crucial role on the interaction between Au nanoparticles and the CeO_2 during the catalytic reaction. Experiments of CO oxidation using bare ceria supports were normalized by BET specific surface area (Figure 3B) and CeO_2-c appeared to be the most active, followed by CeO_2-p and CeO_2-r that showed similar performances. However, the catalytic activity of the Au/CeO_2 catalysts was much superior to that of the CeO_2 supports.

The results of COPrOx experiments, shown in Figure 4, follow analogous trends for CO oxidation. The values obtained for the conversion and selectivity to CO prove that Au/CeO_2-r show the best catalytic performance (Figure 4A), following an identical order previously observed for the oxidation of CO: Au/CeO_2-r > Au/CeO_2-p > Au/CeO_2-c. As reported elsewhere, in the COPrOx experiments the CO conversion increased with respect to the experiments performed in the absence of hydrogen due to the formation of active –OH species at the interface between Au and ceria [9,48]. The half-conversion of CO was achieved at T_{50}=351 K for Au/CeO_2-r, with a CO selectivity of 85%; Au/CeO_2-p realized the half-conversion of CO at 375 K, with 57% selectivity, and Au/CeO_2-c required 424 K to achieve the half-conversion of CO, showing a selectivity of 50%. Our results are in accordance to previous works studying the morphology effects in Au/CeO_2 catalysts in various oxidation reactions, such as CO oxidation and COPrOx [14,36] and in the water-gas shift reaction [24]. Regarding the CO selectivity, the value for Au/CeO_2-r (Figure 4A) stayed constant around 85% up to 353 K and then

started to decrease with higher temperatures of reaction, while for Au/CeO_2-p and Au/CeO_2-c the CO selectivity was considerably lower and diminished as soon as the temperature started to increase. Finally, COPrOx experiments using bare ceria supports (Figure 4B) showed again the order: CeO_2-c > CeO_2-p > CeO_2-r, but with a much lower activity.

3.3 Surface characterization

X-ray photoelectron spectroscopy was used to characterize the near surface region of the samples by recording the high resolution spectra of Ce 3d, O 1s and Au 4f photoelectrons. Figure 5 shows the spectra corresponding to the Ce 3d region, which can be fitted well taking into account the presence of both Ce(III) and Ce(IV) species, as indicated in the figure. For the bare CeO_2 nanoshaped supports the ratio between Ce(III) and Ce(IV) varies from Ce(III)/Ce(IV)=0.34 (CeO_2-c) to 0.43 (CeO_2-r) and 0.46 (CeO_2-p). After deposition of Au, these surface atomic ratios vary considerably depending on the ceria nanoshape. In Au/CeO_2-c, the Ce(III)/Ce(IV) ratio decreases slightly (from 0.34 to 0.28), whereas in Au/CeO_2-p and Au/CeO_2-r the amount of Ce(III) increases up to Ce(III)/Ce(IV) values of 0.54 and 0.64, respectively. In the case of the ceria nanorods, the incorporation of Au results in a notable increase of 50% of the Ce(III) species with respect to the bare support. Then, the presence of Au provokes the reduction of the ceria surface, and this effect depends on the plane of ceria exposed.

The changes in the oxidation state of Ce correlate well with the relative intensity of different lattice oxygen species at the surface and/or subsurface. Figure 6 shows the O 1s spectra of the different samples, which are deconvoluted in three signals. The band at 532.8 eV corresponds to hydroxyl groups whereas those at 528.9 and 530.5 eV are ascribed to ceria lattice oxygen in different coordination environments. It is expected that oxygen atoms interacting with Ce(III) emit photoelectrons at a lower binding energy

than oxygen atoms interacting with Ce(IV). Figure 7 shows a graph where the Ce(III)/Ce(IV) ratios are plotted against the respective ratios between the O 1s signal at 528.9 eV associated to the Ce(III)-O interaction and that at 530.5 eV associated to Ce(IV)-O. There is a clear trend between these surface atomic ratios determined by XPS, which provides an additional proof of consistent interpretation. On the other hand, the graph allows highlighting the effect of Au addition since the different nanoshaped ceria supports cluster in the same area in the plot whereas Au/CeO_2 catalysts span widely in it.

If the presence of Au on CeO_2 is responsible for the partial reduction of the ceria surface, then an electron density transfer from metallic Au towards ceria would result in the partial oxidation of Au or, alternatively, there should be a transfer of oxygen from ceria to Au. Figure 8 corresponds to the Au 4f spectra recorded over the Au/CeO_2 catalysts. The spectrum recorded over the Au/CeO_2-c sample can be fitted by a doublet with bands centered at 84.0 and 87.5 eV, which correspond well with the $4f_{7/2}$ and $4f_{5/2}$ signals of metallic Au. The presence of solely metallic Au is in accordance with the fact that no reduction of the ceria surface occurs in CeO_2-c upon incorporation of Au, as explained above. In contrast, the Au 4f spectra of catalysts Au/CeO_2-p and Au/CeO_2-r contain bands due to both reduced and oxidized Au species. Bands at 84.0 and 87.5 eV correspond to metallic Au whereas bands at 85.8 and 89.3 are ascribed to $4f_{7/2}$ and $4f_{5/2}$ photoelectrons of oxidized Au (Figure 8). These two catalysts, Au/CeO_2-p and Au/CeO_2-r, are exactly the samples that show a significant larger amount of Ce(III) with respect to their corresponding CeO_2-p and CeO_2-r supports, thus confirming that the reduction of the ceria surface is accompanied by a concomitant oxidation of Au. Moreover, catalyst Au/CeO_2-r, which shows the highest amount of Ce(III), also shows the highest degree of Au oxidation (Au(0)/Au(ox)=0.28 for Au/CeO_2-r vs. 0.92 for Au/CeO_2-p). Interestingly, the results observed here for supported Au on different nanoshaped ceria supports appear to be driven in a similar way to the redox interaction

of Cu species (i.e. Cu(II), Cu(I) and Cu (0)) between Ce(III)/Ce(IV) of the ceria support with different morphologies for CO oxidation [15,19,21], COPrOx [20] and water-gas shift reactions [25]. However, the relative ratios of Cu species were not only affected by the exposed surface of ceria support but also by a dynamic chemical change as a function of the temperature and the ratio of reactants during the catalytic process. In particular, catalytic CO oxidation occurred only when surface Cu(I) species were dominant and Cu (0) was scarce [19]. In contrast, the resistance of Au to chemical changes during the catalytic process unlike Cu indicates that the observed changes of Au species are mostly influenced by the different morphologies of the ceria supports.

These are noticeable results considering that we have used strictly the same Au nanoparticles for the preparation of the catalysts and highlights the strong influence of the different ceria facets exposed. Exactly the same nanoparticles were used in a previous work for preparing Au/TiO_2 catalysts and the measurement of Au by XPS showed only the presence of metallic Au [49]. Thus, the oxygen donation capability of ceria is responsible for the oxidation of Au in Au/CeO_2 catalysts, and this capability depends strongly on the geometry of the exposed surface. The {100} surface of ceria in CeO_2-c, which has reported to be the most unstable one [17], is the most active for CO oxidation and COPrOx reaction among the different planes exposed by nanoshaped ceria, in accordance to that reported in the literature after normalizing by surface area exposed [34,35]. However, the {100} surface of CeO_2 does not experience electron transfer with the preformed Au nanoparticles, so Au is kept metallic and the amount of Ce(III) species is low and, consequently, the catalytic performance of Au/CeO_2-c is poor. In contrast, the {110} surface of ceria in CeO_2-r strongly interacts with the preformed metal Au nanoparticles and oxidize them to a large extent, resulting in a high concentration of Ce(III) species at the surface and an extremely Au/CeO_2-r active catalyst. The Au/CeO_2-p catalyst shows an intermediate character in both the amount of oxidized Au and Ce(III) and catalytic activity. Here we have unambiguously

demonstrate that, for a fixed Au nanoparticle size, the Au-ceria interface is strongly influenced by the ceria plane exposed which, in turn, finally determines the final oxidation state of Au and Ce and the catalytic performance.

4. Conclusions

Ceria polycrystals, nanocubes and nanorods were used as supports for anchoring preformed Au nanoparticles and were tested in the CO oxidation and COPrOx reaction. The use of preformed Au nanoparticles allowed preparing Au/CeO_2 catalysts with different ceria nanoshapes but with exactly the same Au dimensions. In contrast to previous works, the use of preformed Au nanoparticles allowed for a careful evaluation of the effect of the exposed planes of ceria on catalytic performance, without introducing new variables related to Au particle size and/or geometry. HRTEM confirmed the existence of only Au nanoparticles of 4.5-5.5 nm in diameter in all the Au/CeO_2 catalyst prepared and the prevalence of {111} facets in the ceria polycrystals, {110} facets in the ceria nanorods, and {100} facets in the ceria nanocubes. XPS revealed that Au was present in a metallic state over the ceria nanocubes, as it was initially in the preformed Au nanoparticles. However, on the ceria polycrystals and especially on the ceria nanorods, there was a very strong interaction between Au and ceria resulting in an electron density transfer from Au to Ce, which ultimately lead to the partial oxidation of Au and to the partial reduction of Ce(IV) into Ce(III). These species, or the existence of a particular Au(ox)-Ce(III) architecture, were much more active in the oxidation of CO and COPrOx. A perfect trend between amount of Ce(III) species, amount of oxidized Au, and catalytic activity has been demonstrated.

Acknowledgments

References

[1]   T. V. Choudhary, D.W. Goodman, Catal. Today 77 (2002) 65–78.

[2]   O. Korotkikh, R. Farrauto, Catal. Today 62 (2000) 249–254.

[3]   G. Kolb, V. Hessel, V. Cominos, C. Hofmann, H. Löwe, G. Nikolaidis, R. Zapf, A. Ziogas, E.R. Delsman, M.H.J.M. de Croon, J.C. Schouten, O. de la Iglesia, R. Mallada, J. Santamaria, Catal. Today 120 (2007) 2–20.

[4]   N.J. Divins, E. López, M. Roig, T. Trifonov, A. Rodríguez, F. González de Rivera, L.I. Rodríguez, M. Seco, O. Rossell, J. Llorca, Chem. Eng. J. 167 (2011) 597–602.

[5]   T.-S. Nguyen, F. Morfin, M. Aouine, F. Bosselet, J.-L. Rousset, L. Piccolo, Catal. Today 253 (2015) 106–114.

[6]   J.A. Cecilia, A. Arango-Díaz, F. Franco, J. Jiménez-Jiménez, L. Storaro, E. Moretti, E. Rodríguez-Castellón, Catal. Today 253 (2015) 126–136.

[7]   I. Miguel-García, Á. Berenguer-Murcia, D. Cazorla-Amorós, Appl. Catal. B Environ. 98 (2010) 161–170.

[8]   K. Liu, A. Wang, T. Zhang, ACS Catal. 2 (2012) 1165–1178.

[9]   N. Bion, F. Epron, M. Moreno, F. Mariño, D. Duprez, Top. Catal. 51 (2008) 76–88.

[10]   P. Lakshmanan, J.E. Park, E.D. Park, Catal. Surv. from Asia 18 (2014) 75–88.

[11]   C. Rossignol, S. Arrii, F. Morfin, L. Piccolo, V. Caps, J.L. Rousset, J. Catal. 230 (2005) 476–483.

[12]   W. Huang, Y. Gao, Catal. Sci. Technol. 4 (2014) 3772–3784.

[13]   D. Zhang, X. Du, L. Shi, R. Gao, Dalton Trans. 41 (2012) 14455–75.

[14]   X.S. Huang, H. Sun, L.C. Wang, Y.M. Liu, K.N. Fan, Y. Cao, Appl. Catal. B Environ. 90 (2009) 224–232.

[15]   J. Qin, J. Lu, M. Cao, C. Hu, Nanoscale 2 (2010) 2739–2743.

[16]   P.X. Huang, F. Wu, B.L. Zhu, X.P. Gao, H.Y. Zhu, T.Y. Yan, W.P. Huang, S.H. Wu, D.Y. Song, J. Phys. Chem. B 109 (2005) 19169–19174.

[17]   E. Aneggi, J. Llorca, M. Boaro, A. Trovarelli, J. Catal. 234 (2005) 88–95.

[18]   B. Acosta, E. Smolentseva, S. Beloshapkin, R. Rangel, M. Estrada, S. Fuentes, A. Simakov, Appl. Catal. A Gen. 449 (2012) 96–104.

[19]   S. Yao, K. Mudiyanselage, W. Xu, A.C. Johnston-Peck, J.C. Hanson, T. Wu, D. Stacchiola, J.A. Rodriguez, H. Zhao, K.A. Beyer, K.W. Chapman, P.J. Chupas, A. Martínez-Arias, R. Si, T.B. Bolin, W. Liu, S.D. Senanayake, ACS Catal. 4 (2014) 1650–1661.

[20]   W.-W. Wang, P.-P. Du, S.-H. Zou, H.-Y. He, R.-X. Wang, Z. Jin, S. Shi, Y.-Y. Huang, R. Si, Q.-S. Song, C.-J. Jia, C.-H. Yan, ACS Catal. (2015) 2088–2099.

[21]   H. Yang, Y. Pan, Y. Xu, Y. Yang, G. Sun, Chempluschem 80 (2015) 886–894.

[22]   L. Liu, Z. Yao, Y. Deng, F. Gao, B. Liu, L. Dong, ChemCatChem 3 (2011) 978–989.

[23]   N. Yi, R. Si, H. Saltsburg, M. Flytzani-stephanopoulos, Energy Environ. Sci. 3 (2010) 831–837.

[24]   R. Si, M. Flytzani-Stephanopoulos, Angew. Chemie - Int. Ed. 47 (2008) 2884–2887.

[25]   S.Y. Yao, W.Q. Xu, A.C. Johnston-Peck, F.Z. Zhao, Z.Y. Liu, S. Luo, S.D. Senanayake, A. Martínez-Arias, W.J. Liu, J.A. Rodriguez, Phys. Chem. Chem. Phys. 16 (2014) 17183–17195.

[26]   W.I. Hsiao, Y.S. Lin, Y.C. Chen, C.S. Lee, Chem. Phys. Lett. 441 (2007) 294–299.

[27]   I.I. Soykal, B. Bayram, H. Sohn, P. Gawade, J.T. Miller, U.S. Ozkan, Appl. Catal. A Gen. 449 (2012) 47–58.

[28]   H. Wang, L. Zhang, M. Li, Y. Liu, X. Bai, J. Rare Earths 31 (2013) 565–571.

[29]   N.J. Divins, A. Casanovas, W. Xu, S.D. Senanayake, D. Wiater, A. Trovarelli, J. Llorca, Catal. Today 253 (2015) 99–105.

[30]   E. Aneggi, D. Wiater, C. De Leitenburg, J. Llorca, A. Trovarelli, ACS Catal. 4 (2014) 172–181.

[31]   M. Abid, V. Paul-Boncour, R. Touroude, Appl. Catal. A Gen. 297 (2006) 48–59.

[32]   X. Weng, J.K. Cockcroft, G. Hyett, M. Vickers, P. Boldrin, C.C. Tang, S.P. Thompson, J.E. Parker, J.C. Knowles, I. Rehman, I. Parkin, J.R.G. Evans, J.A. Darr, J. Comb. Chem. 11 (2009) 829–34.

[33]   K. Zhou, X. Wang, X. Sun, Q. Peng, Y. Li, J. Catal. 229 (2005) 206–212.

[34]   Z. Wu, M. Li, S.H. Overbury, J. Catal. 285 (2012) 61–73.

[35]   S. Agarwal, L. Lefferts, B.L. Mojet, ChemCatChem 5 (2013) 479–489.

[36]   G. Yi, Z. Xu, G. Guo, K.I. Tanaka, Y. Yuan, Chem. Phys. Lett. 479 (2009) 128–132.

[37]   G. Yi, H. Yang, B. Li, H. Lin, K.I. Tanaka, Y. Yuan, Catal. Today 157 (2010) 83–

88.

[38]   Y. Lee, G. He, A.J. Akey, R. Si, M. Flytzani-Stephanopoulos, I.P. Herman, J. Am. Chem. Soc. 133 (2011) 12952–12955.

[39]   M. Baron, O. Bondarchuk, D. Stacchiola, S. Shaikhutdinov, H.-J. Freund, J. Phys. Chem. C 113 (2009) 6042–6049.

[40]   X. Du, D. Zhang, L. Shi, R. Gao, J. Zhang, J. Phys. Chem. C 116 (2012) 10009–10016.

[41]   N. Yi, R. Si, H. Saltsburg, M. Flytzani-Stephanopoulos, Appl. Catal. B Environ. 95 (2010) 87–92.

[42]   M. Haruta, Catal. Today 36 (1997) 153–166.

[43]   M. Chen, D.W. Goodman, Acc. Chem. Res. 39 (2006) 739–746.

[44]   H.X. Mai, L.D. Sun, Y.W. Zhang, R. Si, W. Feng, H.P. Zhang, H.C. Liu, C.H. Yan, J. Phys. Chem. B 109 (2005) 24380–24385.

[45]   J. Llorca, M. Domínguez, C. Ledesma, R. Chimentao, F. Medina, J. Sueiras, I. Angurell, M. Seco, O. Rossell, J. Catal. 258 (2008) 187–198.

[46]   M. Brust, M. Walker, D. Bethell, D.J. Schiffrin, R. Whyman, J. Chem. Soc., Chem. Commun. (1994) 801–802.

[47]   D.R. Mullins, S.H. Overbury, D.R. Huntley, Surf. Sci. 409 (1998) 307–319.

[48]   F. Romero-Sarria, A. Penkova, T. Martinez, M.A. Centeno, K. Hadjiivanov, J.A. Odriozola, Appl. Catal. B Environ. 84 (2008) 119–124.

[49]   E. Taboada, I. Angurell, J. Llorca, J. Catal. 309 (2014) 460–467.

Figure captions
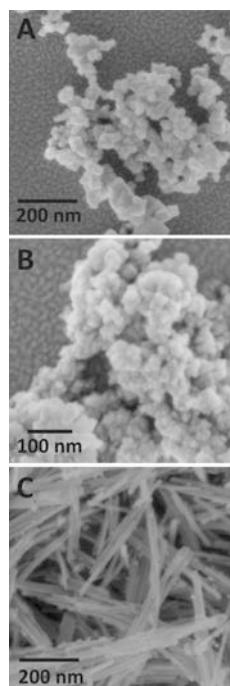
Figure 1. SEM images of nanoshaped ceria supports. A: CeO_2-cubes. B: CeO_2-polycrystals. C: CeO_2-rods.
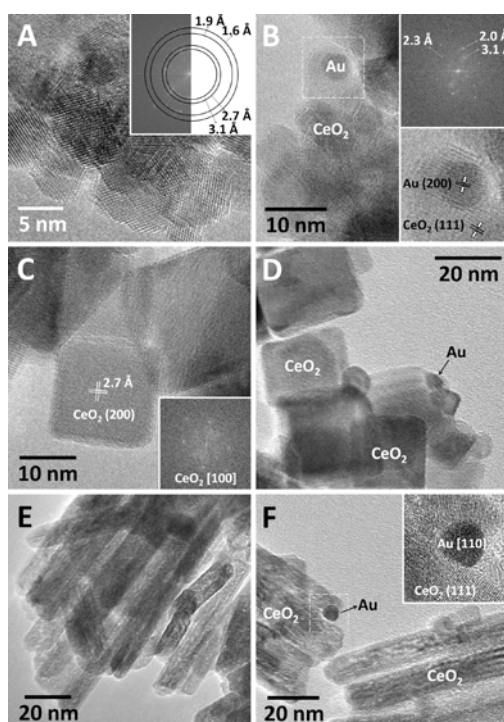

Figure 2. HRTEM images of Au/CeO_2 catalysts and nanoshaped ceria supports. A: CeO_2-polycrystals. The inset shows the FT image for determination of crystallographic planes. B: Au/CeO_2-polycrystals. The top-inset shows the FT image for determination

of crystallographic planes. The bottom-inset shows a detailed magnification of the region comprised within the white dashed line square. C: CeO_2-cubes. The inset shows the FT image for determination of crystallographic planes. D: Au/CeO_2-cubes. E: CeO_2-rods. F: Au/CeO_2-rods. The inset shows a detailed magnification of the region comprised within the white dashed line square.
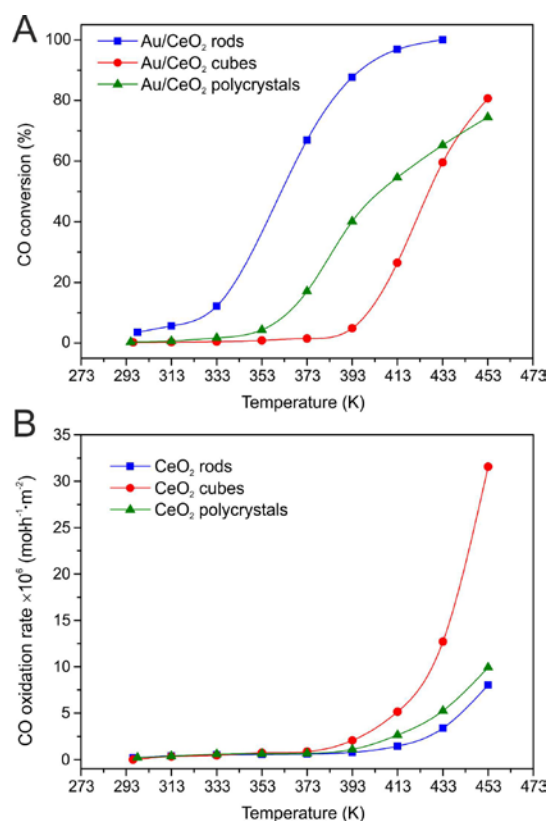
Figure 3. Catalytic performance of CO oxidation. A: CO conversion over nanoshaped Au/CeO_2 catalysts as a function of temperature. B: CO oxidation rate over bare nanoshaped CeO_2 normalized by BET specific surface as a function of temperature.
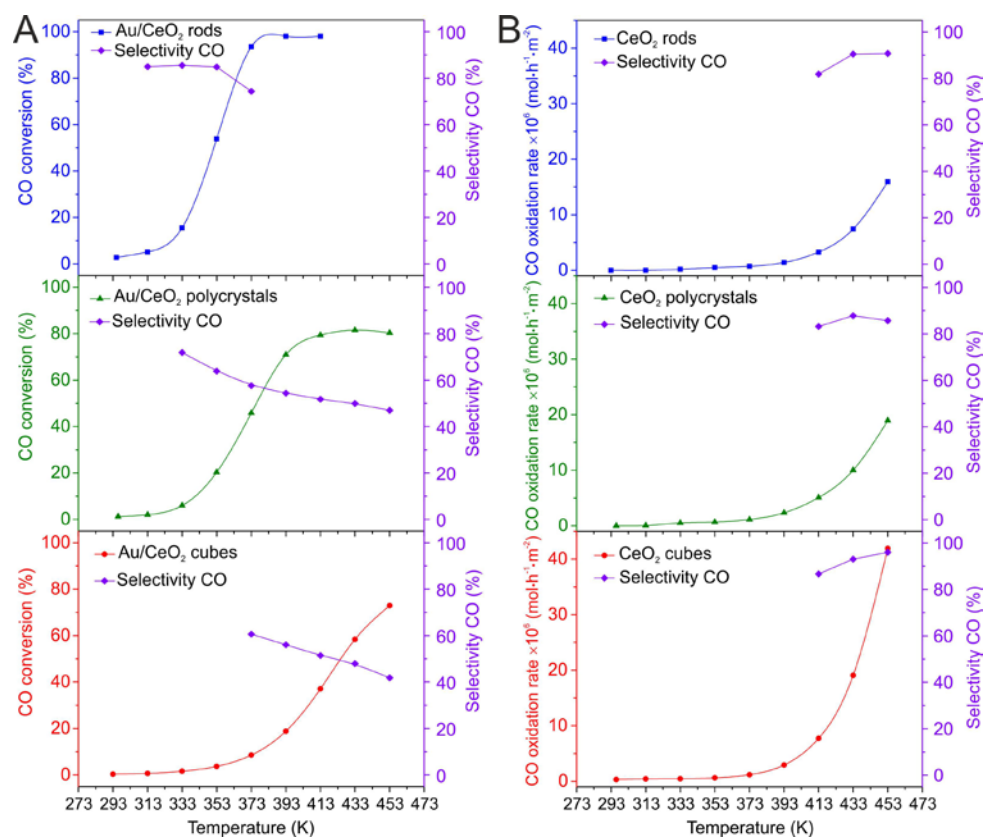
Figure 4. Catalytic performance of COPrOx. A: CO conversion and CO selectivity over Au/CeO₂-r (top plot), Au/CeO₂-p (middle plot) and Au/CeO₂-c (bottom plot) as a function of temperature. B: CO oxidation rate and CO selectivity over bare CeO₂-r (top plot), CeO₂-p (middle plot) and CeO₂-c (bottom plot) normalized by BET specific surface as a function of temperature.
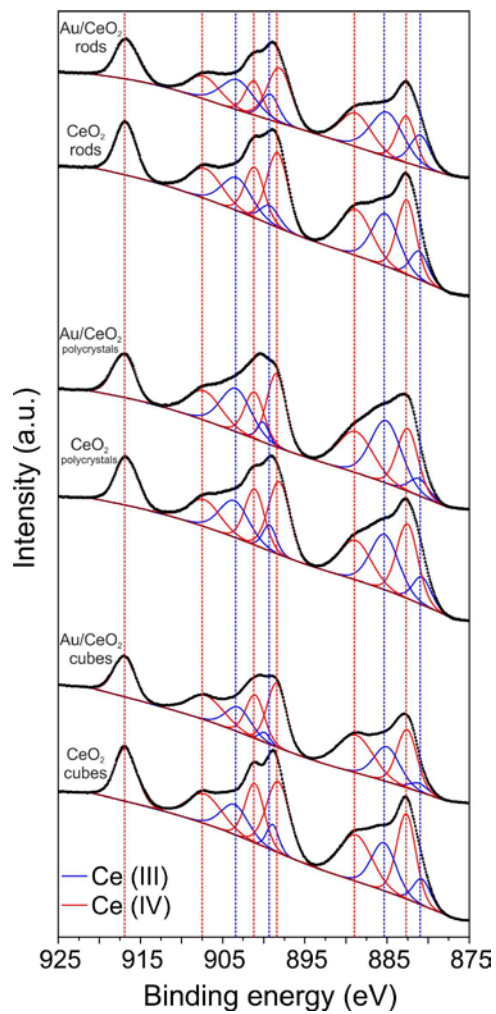
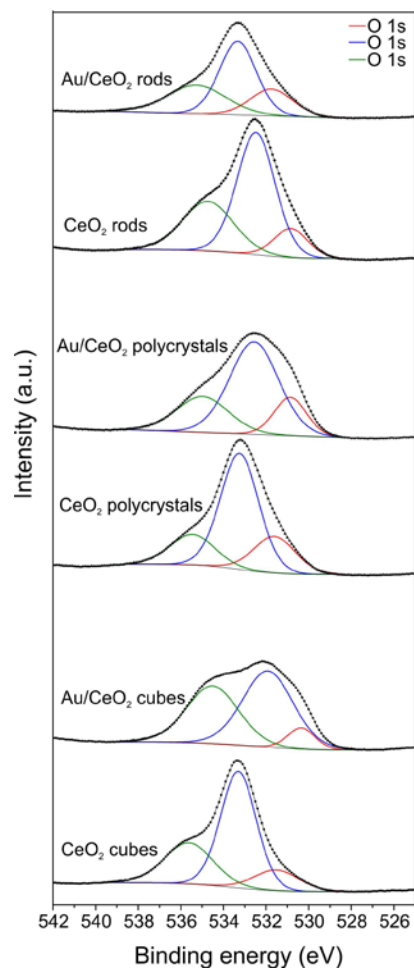Figure 5. XP spectra of the Ce 3d region for Au/CeO$_2$ catalysts and bare CeO$_2$ supports.

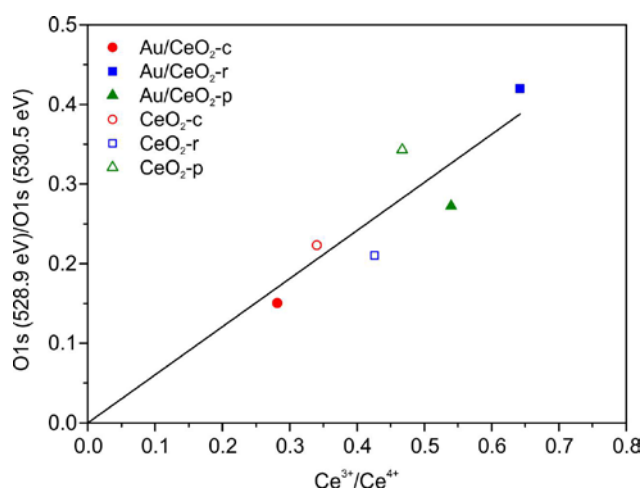Figure 6. XP spectra of the O 1s region for Au/CeO$_2$ catalysts and bare CeO$_2$ supports.

Figure 7. Plot of the Ce(III)/Ce(IV) ratios (Ce 3d) against the ratios of the O 1s band at 528.9 eV relative to the O 1s band at 530.5 eV for Au/CeO$_2$ catalysts and bare CeO$_2$ supports.
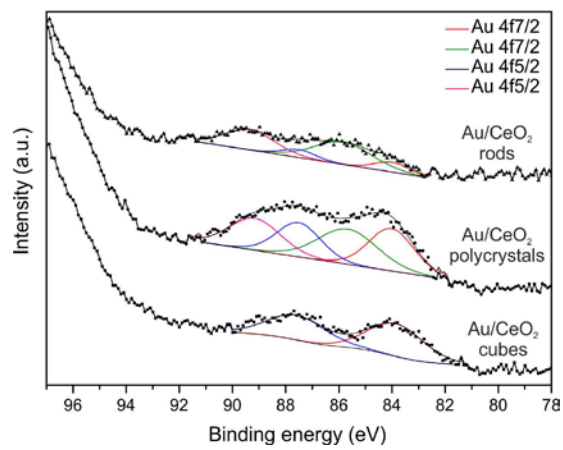
Figure 8. XP spectra of the Au 4f region for Au/CeO$_2$ catalysts.